European Journal of Mechanics B/Fluids 43 (2014) 172–182

Contents lists available at ScienceDirect

European Journal of Mechanics B/Fluids

journal homepage: www.elsevier.com/locate/ejmflu

Experimental analysis of the coherent structures and turbulence past a hydrofoil in stalling condition beneath a water–air interface

Sandro Longo [a,*], Luca Chiapponi [a], María Clavero [b]

[a] Department of Civil Engineering, University of Parma, Parco Area delle Scienze, 181/A, 43124 Parma, Italy

[b] Instituto Interuniversitario de Investigación del Sistema Tierra en Andalucía, Avda. del Mediterraneo s/n, 18006 Granada, Spain

ARTICLE INFO

Article history:
Received 20 May 2013
Received in revised form
14 August 2013
Accepted 28 August 2013
Available online 13 September 2013

Keywords:
Vorticity
Coherent structures
Turbulence near free surface
Experiments
Hydrofoil
Air–water interface

ABSTRACT

In this paper, measurements beneath the interface of the flow past a hydrofoil in water during stalling conditions are used to analyse the mean flow and, in more depth, the large eddies and turbulence. The properties of the time-averaged flow are analysed. In addition to the classical wake, with a recirculation area near the low pressure side of the hydrofoil, a breaker develops due to the limited distance between the hydrofoil and the interface, which causes the generation of further vorticity. Vorticity develops in the recirculation area and at the trailing edge as well. The fluctuating streamwise and transverse velocity demonstrate a classical distribution with maxima at the edge of the wake and beneath the breaker. A quadrant analysis of the Reynolds shear stress indicates the main flux of the momentum, which is always directed towards the axis of the wake to reduce the defect velocity of the wake. The spatial correlations for the longitudinal and transverse fluctuating velocity are computed at several points along the axis of the wake at four different locations downstream. The correlation of the transverse fluctuating velocity shows an evident anisotropy, which is more extensive in the transverse direction and is limited in the streamwise direction. In the streamwise direction, the correlation of the transverse fluctuating velocity also assumes negative values. The correlation of the longitudinal fluctuating velocity is significantly isotropic, and the associated length scale increases downstream. The shape of this last correlation can be fitted with a limited number of eddies; hence, a stable and repetitive pattern of eddies is predicted, as shown in the wavenumber longitudinal and transverse spectra as well.

0. Introduction

Inhomogeneous shear flows represent a wide class of practical flows that require a more detailed analysis than homogeneous turbulent flows. Inhomogeneities arise from the flow boundaries and from the mechanism of energy transfer to turbulence. In some cases it is possible and convenient to analyse separately the large eddies, which are strongly tied to the inhomogeneity, and the main turbulent motion, which is filled with small, quasi-homogeneous eddies. This analysis may be convenient in the near- and intermediate-wake flow past aerofoils and hydrofoils. This wake has been widely studied and has received the attention of many researchers due to the implications in fundamental research on turbulence and the practical applications for optimal performances in aeroplane, marine and submarine vehicles. Coherent structures develop in the near-wake region where numerous phenomena take place and are responsible for mechanical vibrations and noise. Then, these coherent structures transfer energy to the small eddies and gradually disappear in the far wake, where other coherent structures can be generated due to the 'engulfing' of the external region by the wake. Among the coherent structures, often categorised into 'eddies', 'spots', 'slugs' and 'puffs' according to some specific properties, large eddies are of primary interest in the present analysis.

Large eddies, having sizes on the order of the size of the system, were first postulated by Grant [1] and Keffer [2] referring to wakes. Eddies and coherent structures are responsible for the efficient mixing and momentum or chemical transfer, the transfer of energy at small scales through the cascade mechanism, and the production of turbulent energy whenever there is an interaction with shear. Since the early identification of coherent structure in mixing layers by Brown and Roshko [3], there have been studies on eddies and coherent structures in numerous flow fields. Coherent structures generate most of the turbulent shear stress even in homogeneous turbulence, and disregarding the presence of the families of eddies does not, as a consequence, satisfy some common assumptions, such as when modelling the turbulence stresses in terms of the mean velocity gradients using the eddy viscosity. Additionally, the dissipation, though mainly due to very small

* Corresponding author. Tel.: +39 0521 90 5157; fax: +39 0521 90 5924.
E-mail addresses: sandro.longo@unipr.it (S. Longo), luca.chiapponi@unipr.it (L. Chiapponi), mclavero@ugr.es (M. Clavero).

0997-7546/$ – see front matter © 2013 Elsevier Masson SAS. All rights reserved.
http://dx.doi.org/10.1016/j.euromechflu.2013.08.007

Nomenclature

$\overline{\cdots}$	Time average operator, ensemble average operator
$\widehat{\cdots}$	Phasic average operator
α	Angle of attack, angle of the mirror, energy coefficient
$\varepsilon_{(\cdots)}$	Uncertainty, absolute value
ϕ	Phasic indicator
ρ	Mass density
η	Transverse non-dimensional coordinate for the wake
κ	Turbulent kinetic energy
ν	Kinematic viscosity
$\sigma_{(\cdots)}$	Uncertainty, relative value
ω_z	Component of vorticity in the spanwise direction
χ_{ij}	Spatial correlation
Λ_l, Λ_t	Integral longitudinal length scale, transverse length scale
b	Parameter, shift of an eddy
C	Cord length, concentration, coefficient
d	Water depth upstream of the aerofoil
dT	Interval time between two coupled frames in PIV
E_{ij}	Power spectrum of turbulence
f_{acq}	Frequency of acquisition
FOV	Field of view
Fr, $\mathrm{Fr_{le}}$, $\mathrm{Fr_{te}}$	Froude number, computed by using the water depth respect to the leading edge or respect to the trailing edge
h	Trailing tip elevation respect to the bottom of the flume
h_{le}, h_{te}	Water depth respect to the leading edge, the trailing edge
H	Threshold in quadrant analysis
i_f	Bottom inclination
$\mathbf{k}$, k_x, k_y	Wavenumber vector, component in direction x and y
$k_{x\mathrm{min}}$, k_{xc}	Minimum wavenumber, cut off wavenumber
L_0	Transverse length scale of the wake
N	Number of elements (events) in the sample
N_i	Number of elements (events) belonging to the ith quadrant
PIV (DPIV)	Particle Image Velocimetry (Digital)
PID	Proportional–Integral–Derivative feedback system
PMMA	Polymethyl methacrylate
Q	Water discharge
R^2	Coefficient of determination
R_{ij}	Coefficient of correlation
Re	Reynolds number, based on the chord length and on kinematic viscosity
t	Time
TKE	Turbulent kinetic energy
U_0	Asymptotic upstream velocity
U, V	Streamwise, transverse velocity
U_{le}, U_{te}	Streamwise velocity referred to the leading edge section, to the trailing edge section
U', V'	Streamwise, transverse fluctuating velocity
x, y	Spatial coordinates
X_W	Horizontal size of the interrogation window

eddies at a scale where homogeneity is a common assumption, appears to take place in patches instead of being a continuum. The presence of eddies past bluffs or streamlined bodies is well known and has been widely investigated. For hydrofoils, the eddies detach at the edges and are convected downstream, carrying vorticity.

The specific geometry chosen for the experiments, which is with a hydrofoil in water at a small distance beneath the air–water interface (and which is not the one used for hydrofoils in marine vehicles, since we were interested in different phenomena with respect to lift, drag etc.), allows the interaction of the wake with the interface and further vorticity, and eddies that are generated are similar to those obtained in a stationary spilling breaker. Spilling breakers are typical of deep ocean waves and hydraulic jumps (see [4,5] for an overview of the principal features of these types of breakers) and are often obtained through a hydrofoil beneath a free surface [6–9]. A spilling breaker exhibits a roller near the crest, a turbulent region beneath the free surface or a combination of both [9]. In the present experiments a distance of 57 mm between the midchord of the hydrofoil and the free surface still guarantees the existence of a flow of limited vorticity between the wake of the hydrofoil and the free surface. The presence of the interface is itself a source of inhomogeneity because the large eddies are partially constrained in their size depending on their distance from the interface.

Similar devices, with a different geometry, have practical applications also in industrial processes as mixer elements and in blades.

In this paper, we use DPIV techniques to measure the velocity past the hydrofoil and near the free surface to analyse large eddies, main turbulent motion and small eddies. Despite the large number of video camera pixels, we could not cover all the field of interest with a single image, which is elongated and extends for several chord lengths downstream; hence, we decided to conduct a series of measurements in identical conditions to collect a mosaic of individual frames. Because each frame (or series of frames) is a realisation and because each realisation is inherently different, specific attention was paid to building up the flow statistics through ensemble averaging.

The paper is organised as follows. After the description of the experimental set-up in Section 1, Section 2 describes the mean flow and the main turbulent flow, including the quadrant analysis of the Reynolds shear stress. Section 3 is devoted to the spatial correlation and the linear spectra analysis. The conclusions are reported in the final section.

1. Experimental set-up

The experiments were conducted in the flume in the Laboratory of Hydraulics of the Department of Civil Engineering (DICATeA) of the University of Parma, Italy. The flume is 0.30 m wide, 0.45 m high and 10 m long; the sidewalls are made of glass; the bottom is stainless steel. A flow straightener at the entrance eliminates the large-scale vortices and eddies, and a bottom-hinged flap gate at the downstream end of the flume allows control of the water level. To circulate the water stored in three tanks, there is a centrifugal pump, and a PID regulator that controls an electric valve diverts part of the flow and guarantees the stability of the desired flow rate in the flume. The flow rate is measured by a Promag Hendress–Hauser magnetic flow meter, with an accuracy of 0.5% of the instantaneous measured value. The variability in the flow discharge is less than 0.1 l/s. In the present tests, the bottom inclination is $i_f = 1\%$. The Reynolds number of the water stream, which is based on the hydraulic radius, is equal to 38 900, and the Froude number is $\mathrm{Fr} = 0.26$; hence, the water flow is turbulent and is in a subcritical regime. The measured free stream turbulence in the midsection of the flume is equal to 5%. The water used in the experiments is tap water seeded with silt, which has a size of 10–20 μm, to facilitate the subsequent acquisition of information using the DPIV. The relaxation time of the particles (see [10]) is less than 10^{-3} s, hence the particles are well suited to follow the water particles in the present experimental conditions. The NACA profile

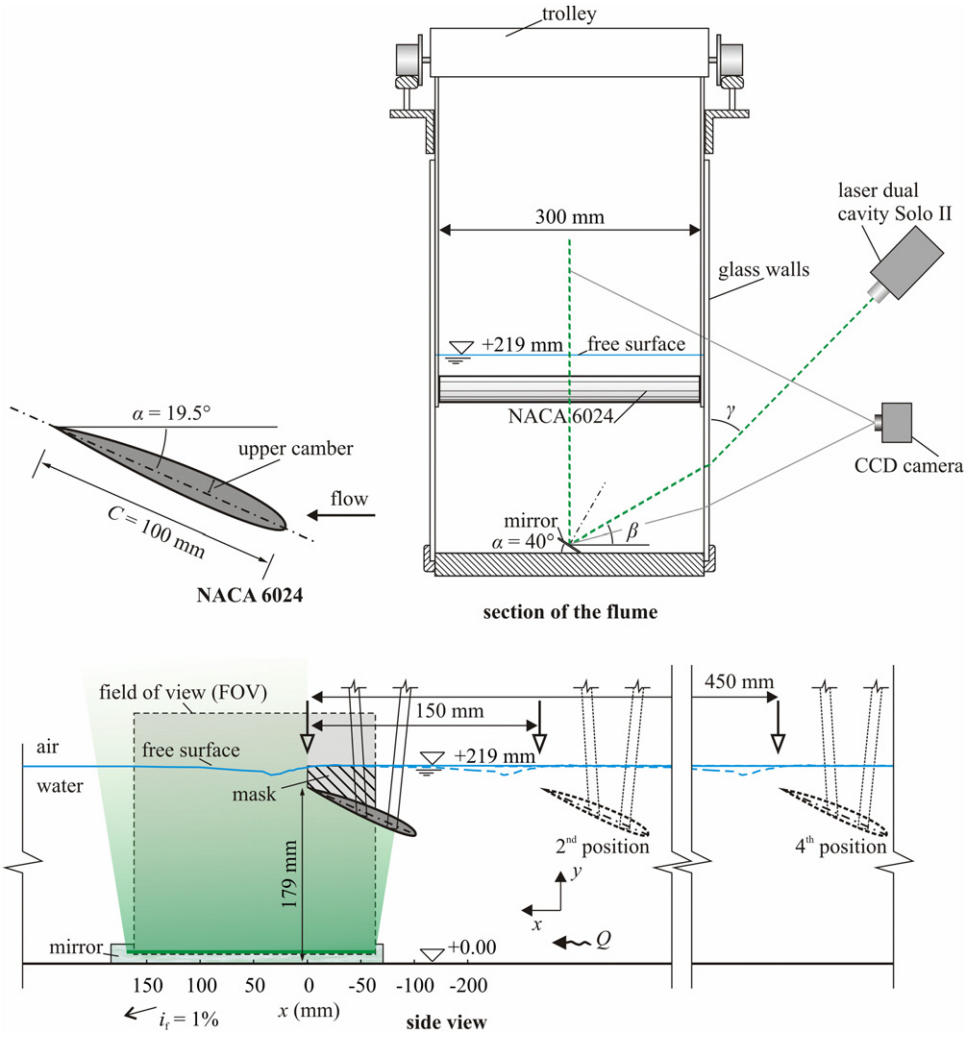

Fig. 1. Overview of the experimental system for experiment 3.

belongs to the four digit series 6024, is asymmetric and is achieved using polymethyl methacrylate (PMMA) with a milling machine. The overall accuracy of the profile surface is 1/10 mm; the chord length is 100 ± 1 mm; the maximum thickness is 24 mm; and the span is 298 mm. The profile is supported by an aluminium frame of limited invasivity, with the struts supporting the hydrofoil close to the two sidewalls, and is connected to a trolley moving on two railways at the top of the flume. The trolley can be moved with a referenced position using a rule fixed to the railways.

Measurements were carried out using a TSI PIV with a 2048 × 2048 pixel video camera (TSI Power View Model 630149) fitted with a NIKKOR AF D 50 mm/f lens with an adapter ring (Nikon PK-12), which increases the focal distance by 14 mm. The light source was a Solo Nd:YAG III dual laser head with a maximum repetition rate of 15 Hz and an output energy of 50 mJ. The laser was water cooled and mounted on the same side of the video camera. The layout is shown in Fig. 1.

Polarised filters were added to the video camera to eliminate the reflections. The acquisition frequency for an image couple was 3.75 Hz with a time interval between the two images of 2000 μs. Because the bottom of the flume is not transparent, a mirror was positioned to reflect the laser sheet coming from a sidewall. Shadowing by the hydrofoil prevented PIV data acquisition on the foil's pressure side for $x/C > 0$.

The calibration of the PIV gave a resolution of 0.11 mm per pixel. Velocity computation was carried out using a correlation analysis of two different frames through the use of an interrogation window of 32 × 32 pixels with a 50% overlap. The result is a matrix of vectors at the grid nodes, which are 16 pixels apart and correspond to 1.81 mm in the longitudinal and in the transverse direction. After the correlation analysis was complete, outliers were rejected using the cellular neural network method [11]. The percentage of vectors rejected varied from 6% to 16%. For each test, 1000 frame couples were acquired, which corresponds to approximately 267 s. During the experiments, the water temperature was monitored but not controlled. The mean water temperature was between 26 °C and 27.2 °C, with 0.8 °C variations at most for the tests of the same experiment.

In addition to the PIV quantitative approach, qualitative information was gained by flow visualisation and acquisition of the image with a digital camera and a digital HD video camera (see the videos in the annexes). Fig. 2 shows two photographs with the wake visualised using methylene blue injected by a needle to enhance the coherent structures. The slight turbulence of the incoming stream is observed in the geometry of the dye. The spilling breaker (similar to a hydraulic jump) is evident downstream. The Reynolds number refers to the chord length. A detail of the breaker is shown in Fig. 3. The mixing process starts past the toe and clearly brings the tracer in contact with the free surface after incorporation into an eddy.

The two-dimensionality of the flow has not been directly verified, but some specific tests [12] on a hydrofoil with the same

Table 1
Experimental parameters. d is the water depth upstream of the hydrofoil, h is the trailing tip elevation respect to the bottom of the flume, U_0 is the asymptotic velocity, α is the hydrofoil attack angle, $\mathrm{Re} = U_0 C/\nu$ is the Reynolds number based on the chord length $C = 100 \pm 1$ mm, f_{acq} is the frequency of acquisition of the PIV, dT is interval time between the two coupled frames.

Test #	d (mm)	h (mm)	U_0 (m/s)	α (°)	Re	f_{acq} (Hz)	No frames	dT (μs)
3	219 ± 1	179 ± 1	$0.381 \pm 1.5\%$	19.5	45 500	3.75	1000	2000

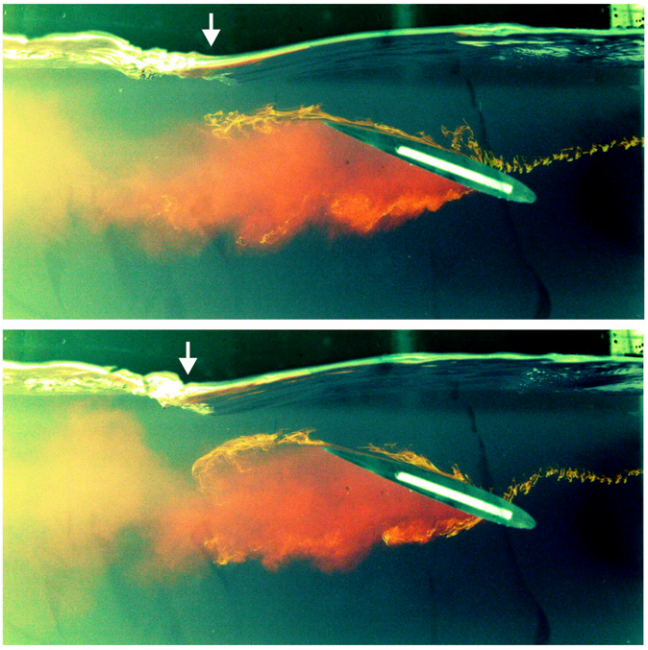

Fig. 2. Two photographs of the hydrofoil with the wake visualised using methylene blue injected on the right side. The breaker is evident on the left. The interval time between the two frames is 0.33 s. $\mathrm{Re} = 44\,500$ and $\alpha = 19.5°$.

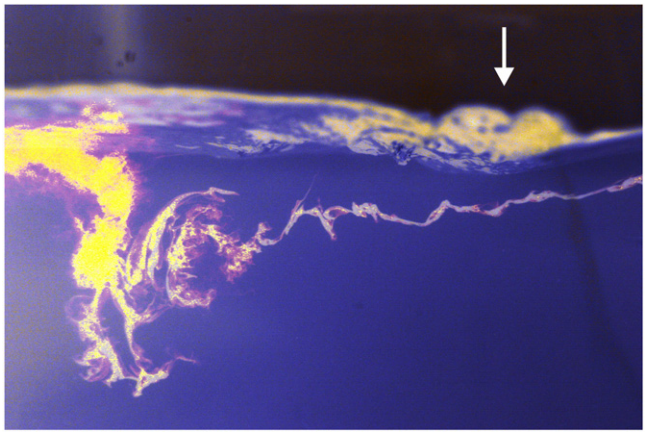

Fig. 3. Detail of the breaker. The tracer is methylene blue injected near the free surface. The mixing starts downstream past the toe.

span-to-chord ratio as the present experiments (3 to 1) and with a similar Reynolds number shows that the three-dimensional effects are limited to the thickness of the wall boundary layer and are on the order of a few centimetres. Therefore, the free stream velocity field is indeed two-dimensional over the centre portion of the hydrofoil, where the measurements were performed.

The flow field measurements are conducted for four different Reynolds number. The velocity measurement domain is $181 \times 145 \times 1$ mm^3 (W, H, D) in each FOV. Experiment 3 included four subsequent FOVs with an overlap of 31 mm. The measurement domain is smaller than the acquisition domain due to frame cropping. Table 1 shows the experimental parameters for the test.

1.1. Uncertainties in measurements

Uncertainties in the PIV measurements include random and bias errors in the velocity measurements and bias errors in the spatial location of these velocities. With a typical sub-pixel resolution equal to ±0.20 pixels, the uncertainty due to random error in the displacement of the particle is $\sqrt{2} \times 0.20 = 0.28$ pixels and the relative error for a particle displaced 8 pixels is ±3.5%. Because the timing error is negligible, the relative velocity uncertainty has the same value. These estimates were confirmed by measuring the velocity of a rotating disc connected to a stepper. By time averaging over 1000 instantaneous frames, the uncertainty is reduced to ±1%; hence, most of the error was random. Bias errors in the PIV velocities are introduced through uncertainty in image scaling. The calibration was performed using a uniform grid suspended in water in the absence of flow and by detecting four points at the corner of a rectangle having edge lengths of 180 mm along the horizontal side and 135 mm along the vertical side. Assuming an error of ±1 pixel in detecting each grid knots and an accuracy of ±0.5 mm in drawing the grid lines, the overall uncertainty in edge length detection is $\pm|2 \times 0.11 + 0.5| = 0.77$ mm, and the relative value on the minor length is equal to ±0.6%. Therefore, the global uncertainty in the velocity is equal to $\sigma_u = \pm 4.1\%$ for the instantaneous value and is equal to $\sigma_u = \pm 1.6\%$ for the averaged value (1000 frames). If the velocity is expressed in a non-dimensional form, uncertainty is introduced through the normalisation velocity U_0. The normalisation velocity is the far upstream velocity and has been evaluated as the ratio between the flow rate and the section of discharge. The discharge is controlled within 0.1 l/s, and the section of discharge is measured with an uncertainty equal to ±0.5%. For tests at a nominal discharge of 25 l/s the normalisation velocity has an uncertainty of ±0.9%. The instantaneous normalised velocity has an uncertainty of ±5.0%, while the averaged normalised velocity has an uncertainty of ±2.5%. These estimates are overstated for a high velocity and understated for a low velocity.

The spatial derivatives were calculated using a central scheme with an absolute uncertainty of $\varepsilon_{\partial u/\partial x} = \pm 0.7 \varepsilon_u / \Delta x$ [10], where ε_u is the absolute velocity uncertainty and Δx is the interval between the data. The uncertainty concerning the vorticity doubles because it involves two derivatives. For a velocity of 0.38 m/s the uncertainty on the instantaneous derivative is $\varepsilon_{\partial u/\partial x} = \pm 6.1\ \mathrm{s}^{-1}$ and on the instantaneous vorticity is $\varepsilon_{\omega_z} = \pm 12.2\ \mathrm{s}^{-1}$; the uncertainty on the derivative of the mean velocity is $\varepsilon_{\partial \overline{u}/\partial x} = \pm 2.35\ \mathrm{s}^{-1}$ and on the mean vorticity is $\varepsilon_{\overline{\omega}_z} = \pm 4.7\ \mathrm{s}^{-1}$. The uncertainty of non-dimensional vorticity is further increased due to the uncertainty of the normalisation velocity and of the chord length. This last uncertainty can be assumed to be 1%; therefore, for reference, a mean vorticity of $20\ \mathrm{s}^{-1}$ has an uncertainty in the non-dimensional value of 25.4%. The values have been reported to give a proper indication of the global level of uncertainty.

2. The mean flow

In Fig. 4, the time-averaged velocity is shown normalised by the velocity upstream. Two different structures can be observed.

The first is the wake past the aerofoil, which is characterised by a strong defect velocity in the sections located downstream near the body and by a progressive recovery of the uniformity in the

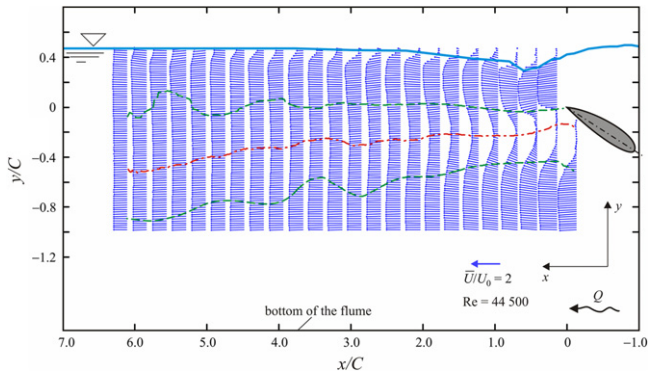

Fig. 4. The time-averaged, measured velocity (undersampled by a factor 15 in the x direction) normalised by the velocity far upstream, U_0. The dash–dot line indicates the local minimum velocity, and the two dashed curves indicate where the defect velocity is half the maximum defect velocity.

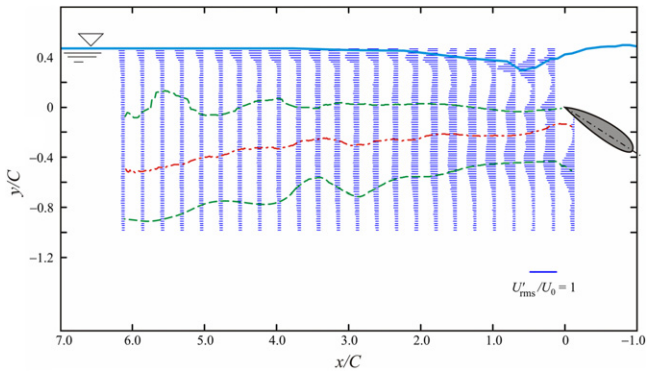

Fig. 5. Streamwise fluctuating velocity (undersampled by a factor 15 in the x direction) normalised by the velocity far upstream, U_0.

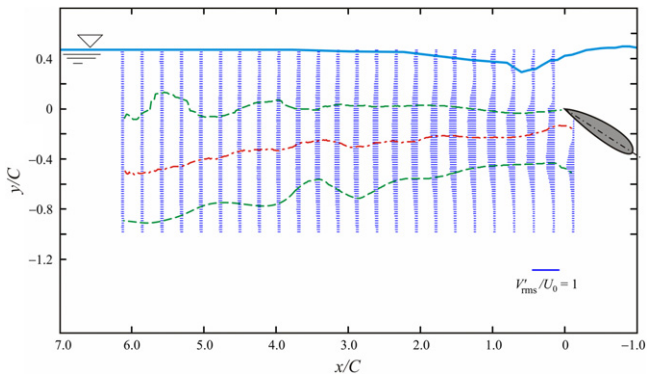

Fig. 6. Transverse fluctuating velocity (undersampled by a factor 15 in the x direction) normalised by the velocity far upstream, U_0.

transverse direction. The dash–dot line represents the axis of the wake, where the defect velocity is maximum. The dashed lines represent the edge of the wake, where the defect velocity is halved with respect to its value along the same vertical. Usually, the distance from the axis where the defect velocity is halved, L_0, is assumed to be the local transverse scale, and in some conditions, the self-similarity is verified with respect to the non-dimensional transverse coordinate $\eta = y/L_0$. The edge of the wake corresponds to $\eta^2 = 1$, and the outer region of the wake corresponds to $\eta^2 > 3$. Note that, especially near the body, the wake is not symmetric because it has a memory of the shape of the body. Additionally, the wake has non-symmetric boundary conditions: a breaker on the upper side and a solid wall in a limited domain on the lower side. The velocity values in the outer region of the wake are much greater than the upstream, undisturbed velocity, with an increment equal to more than 50% in the locations near the hydrofoil. The low pressure side of the hydrofoil is in contact with a recirculation zone where the separation occurs. The high pressure side of the hydrofoil, which faces the free surface, is intersected by an accelerated boundary layer that detaches at the trailing edge and merges with the recirculation zone.

The second structure of the flow field is a stationary breaker at the free surface past the trailing edge. The current above the profile is accelerating and experiences a reduction in the water depth (with respect to the upper face of the profile but also with respect to the bottom of the flume), and the flow profile can be computed by assuming that the current is gradually varying. The exit velocity at the trailing edge is roughly uniform in the vertical and equal to $\overline{U}_{te} = 0.53$ m/s. The relative water depth is $h_{te} = 33$ mm. The local Froude number is $\mathrm{Fr}_{te} = \overline{U}_{te}/\sqrt{gh_{te}} = 0.93$ and the current is nearly at a critical condition. Assuming a negligible dissipation of the stream between the leading and the trailing edge, the energy balance equation is

$$h_{te} + \alpha_{te}\frac{\overline{U}_{te}^2}{2g} = h_{le} + \alpha_{le}\frac{\overline{U}_{le}^2}{2g}, \tag{1}$$

with the constraint being derived from the mass balance equation:

$$h_{te}\overline{U}_{te} = h_{le}\overline{U}_{le}. \tag{2}$$

α_{te} and α_{le} are the energy coefficients to correct the velocity head of the stream for the non-uniform velocity distribution in the vertical direction. Assuming that the coefficients are unitary, applying Eqs. (1)–(2) results in $h_{le} \approx 79$ mm, and the corresponding Froude number at the leading edge is $\mathrm{Fr}_{le} = \overline{U}_{le}/\sqrt{gh_{le}} = 0.25$. The water depth at that location is approximately 6 mm above the undisturbed upstream water depth, which indicates a backwater as a consequence of the presence of the hydrofoil.

The free surface is strongly oscillating with the toe of the breaker and periodically moves with a series of capillary waves upstream with respect to the toe. A detailed analysis of the breaker generated by a submerged hydrofoil is reported in [9], with attention focused on the vorticity evolution beneath the breaker and analysis of the form of the free surface. In Lin and Rockwell, experimental capillary waves develop from the toe for the Froude number that is based on the chord length of the hydrofoil and on the upstream, undisturbed velocity, which is equal to 0.43, and the transition to a developed breaker is completed at a Froude number equal to 0.49. In this respect, we assume that the proper Froude number has to be computed by introducing the local water depth (or the thickness of the shear layer), and the local mean velocity that appears more relevant than the chord of the hydrofoil and the upstream undisturbed velocity in assessing the balance between the convective inertial forces of the flow and the gravitational effects.

The water concentration (it is the ratio between the interval time of presence of water to the total time) is less than unity in the area of the breaker, and the computed velocity is phasic averaged, i.e., only refers to the time interval in which water is present. The breaker triggers a series of waves downstream, which also modulate the wake edge, with a length of less than $2C$.

The two structures of the flow are also reflected in the distribution of the streamwise and transverse fluctuating velocity, as shown in Fig. 5 and in Fig. 6. The wake shows a typical distribution that is almost symmetrical with respect to the axis, at least at locations $x/C > 0.5$, with the streamwise component being slightly greater than the transverse component and with the maximum intensity near the edges. The breaker has the maximum values of streamwise fluctuating velocity at the toe and, while the streamwise turbulence is decaying downstream from the wake, it is persistent beneath the free surface.

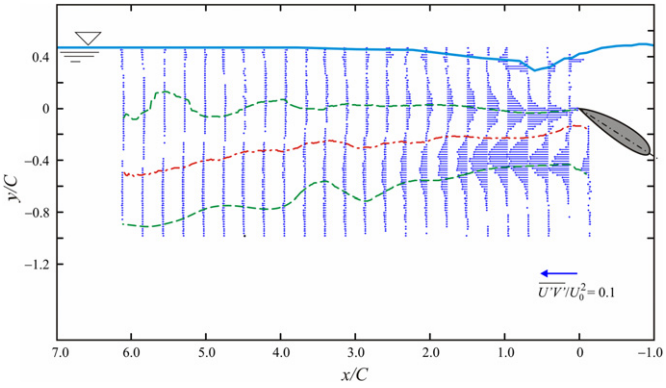

Fig. 7. Reynolds shear stress (undersampled by a factor 15 in the x direction) normalised by the velocity far upstream, U_0.

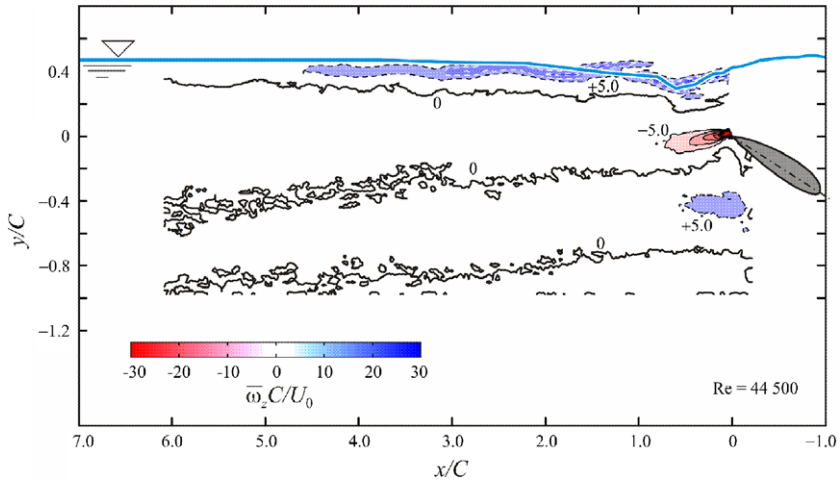

Fig. 8. Non-dimensional vorticity. Contour lines with a step equal to 5. Dashed lines refer to positive (clockwise vorticity).

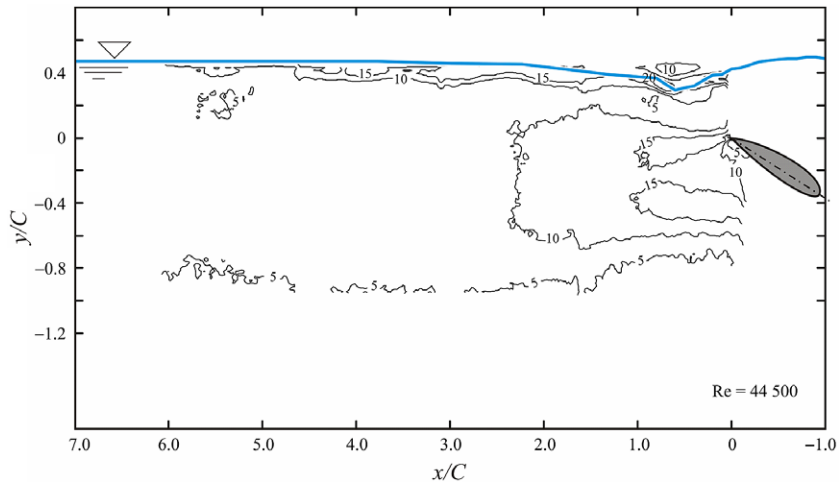

Fig. 9. Non-dimensional root mean square value of the vorticity, $\omega_{z\mathrm{rms}} C/U_0$.

2.1. Turbulence structure

The Reynolds shear stress is shown in Fig. 7 with a typical antisymmetrical distribution for the wake and a spatially modulated pattern near the free surface.

Fig. 8 shows the time-averaged non-dimensional vorticity perpendicular to the plane of the flow. The negative (counterclockwise) and positive (clockwise) vortices are concentrated near the trailing edge and the leading edge. The vorticity has a maximum negative value at the trailing edge and then changes sign and becomes positive in proximity to the breaker, which is beneath the free surface. Persistent positive values are found downstream beneath the free surface and are partially modulated by the pulsating breaker. Near the free surface, the computation of vorticity was performed by masking the air side and inserting a constant velocity in the vertical direction that is equal to the first value recorded in the water. This procedure is necessary to avoid a false shear layer at the interface.

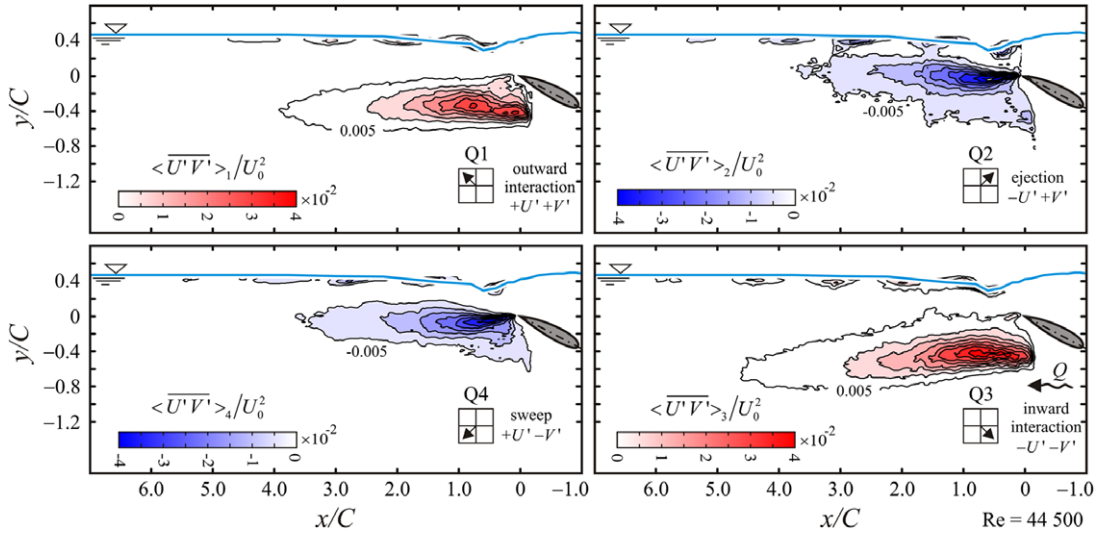

Fig. 10. Time-averaged Reynolds shear stress quadrant decomposed with a threshold $H = 0$. The values are non-dimensional with respect to U_0. The contour lines have a step equal to 0.005.

A measure of the stationarity of the vorticity is the r.m.s. value shown in Fig. 9. The major fluctuations are in the recirculation zone, the trailing edge and beneath the free surface as well. The r.m.s values are generally larger than the mean values and confirm the relevant unsteadiness of all the processes involved in the wake and beneath the free surface.

2.2. Quadrant analysis

Quadrant analysis has been widely used to reveal turbulent structures at the wall boundary layer over a rigid wall [13,14], in turbulent channel flow [15], and in the far turbulent wake of a cylinder [16]; to find the most significant form of the disturbance in a turbulent wall boundary layer [17]; and to analyse the water side boundary layer statistics [18] as well as the air side boundary layer statistics [19] in wind-generated gravity waves [20]. The quadrants are listed with numbers from 1 to 4, where quadrant 1 indicates the positive horizontal axis and the positive vertical axis, quadrant 2 indicates the negative horizontal axis and positive vertical axis etc. The technique separates the contribution of the fluctuating velocity in the Reynolds' tensor according to the sign of the fluctuation. The event-averaged shear stress for the ith quadrant is

$$\langle \overline{U'V'} \rangle_i = \frac{1}{N_i} \sum_{j=1}^{N_i} \left[U'V' \right]_i \quad \text{for } i = 1, \ldots, 4, \tag{3}$$

where N_i is the number of events in the ith quadrant and j is the current sample number. The average shear stress for the ith quadrant is

$$\overline{U'V'}_i = \frac{1}{N} \sum_{j=1}^{N_i} \left[U'V' \right]_i \quad \text{for } i = 1, \ldots, 4. \tag{4}$$

The ratio, N_i/N, is the relative permanence of the events in the ith quadrant; hence,

$$\overline{U'V'}_i = \frac{N_i}{N} \langle \overline{U'V'} \rangle_i \tag{5}$$

and the total shear stress is

$$\overline{U'V'} = \sum_{i=1}^{4} \overline{U'V'}_i. \tag{6}$$

Instead of considering all the data, it is possible to fix an amplitude threshold including only the events satisfying the relation $|U'V'| > T$, where T is usually defined in terms of the root-mean-square stress:

$$|U'V'| > H \left(U'_{\text{rms}} V'_{\text{rms}} \right) \tag{7}$$

where H is a threshold. The concentration of the ith quadrant for a fixed threshold level is

$$C_H^i = \frac{1}{N} \sum_{j=1}^{N} \phi_{H,j}^i, \tag{8}$$

where

$$\phi_{H,j}^i = \begin{cases} 1 & \text{if } |U'V'|_j > TH \text{ and belongs to the } i\text{th quadrant} \\ 0 & \text{otherwise.} \end{cases} \tag{9}$$

We can also consider the phasic-averaged Reynolds stress for the ith quadrant:

$$\left(\widehat{U'V'} \right)_H^i = \frac{\sum_{j=1}^{N} \left(U'V' \right)_j \phi_{H,j}^i}{\sum_{j=1}^{N} \phi_{H,j}^i} \tag{10}$$

and the time-averaged Reynolds stress for the ith quadrant:

$$\left(\overline{U'V'} \right)_H^i = \frac{1}{N} \sum_{j=1}^{N} \left(U'V' \right)_j \phi_{H,j}^i = C_H^i \left(\widehat{U'V'} \right)_H^i. \tag{11}$$

The non-dimensional quadrant contributions without threshold are shown in Fig. 10. Due to the symmetry in the wake, the contributions of Q2 and Q4 are dominant in the upper lobe, with a peak at $x/C = 0.35 \div 0.5$, and the contributions of Q1 and Q3 are dominant in the lower lobe, with a peak at $x/C = 0.75$. The maximum absolute contribution is similar for both lobes, but the lower lobe wake is characterised by a more persistent transfer of momentum. Beneath the free surface, all the contributions from the quadrants are spatially modulated following the steady wave pattern of the free surface.

The results obtained for $H = 1$ are shown in Fig. 11. The pattern is similar to the situation where $H = 0$, but the stresses are one

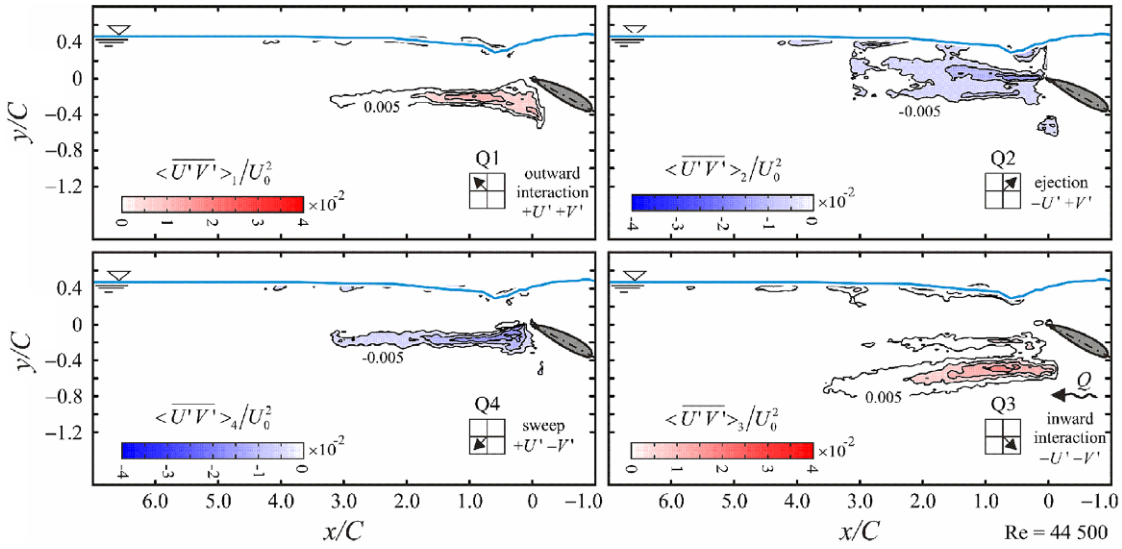

Fig. 11. Time-averaged Reynolds shear stress quadrant decomposed with threshold $H = 1$. The values are non-dimensional with respect to U_0. Contour lines have a step equal to 0.005.

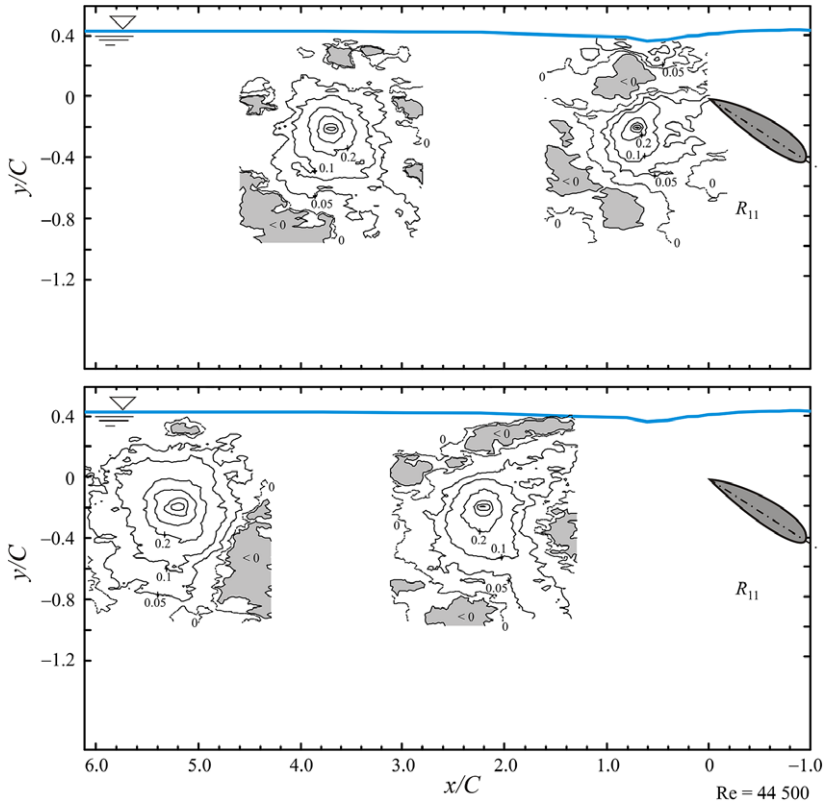

Fig. 12. Correlations for the longitudinal fluctuating velocity computed at $x/C = 0.7, 2.2, 3.7, 5.2$ for points along the axis of the wake.

order of magnitude less. Because it is a time average, by increasing the threshold, the events are stronger but their duration is progressively much shorter. Ejections (Q2) and sweeps (Q4) dominate the upper boundary of the wake, beneath the free surface, while outward (Q1) and inward (Q3) interactions dominate the lower boundary of the wake. The inward interaction has greater values and extension and is the most relevant mechanism of stress transfer towards the centreline of the wake. Notably, the distribution of the quadrant-dependent stress indicates that the stress acting on the upper lobe of the wake is only due to Q2–Q4 events (the other quadrants give a negligible contribution), while stress on the lower lobe is only due to Q1–Q3 events (in this case the other quadrants give a negligible contribution as well). By increasing threshold for the time-average, the values are dampened slightly, but their localisation is essentially invariant. Therefore, the events are strongly localised and can be attributed to the permanent mean pattern of the fluid flow.

3. Spatial correlations and spectra

A measure of the spatial structure of the flow field is represented by the spatial correlation tensor. The double velocity spatial correlation is

$$\chi_{ij}(\mathbf{x}, \mathbf{x}+\mathbf{r}) = \overline{U_i'(\mathbf{x}) U_j'(\mathbf{x}+\mathbf{r})} \tag{12}$$

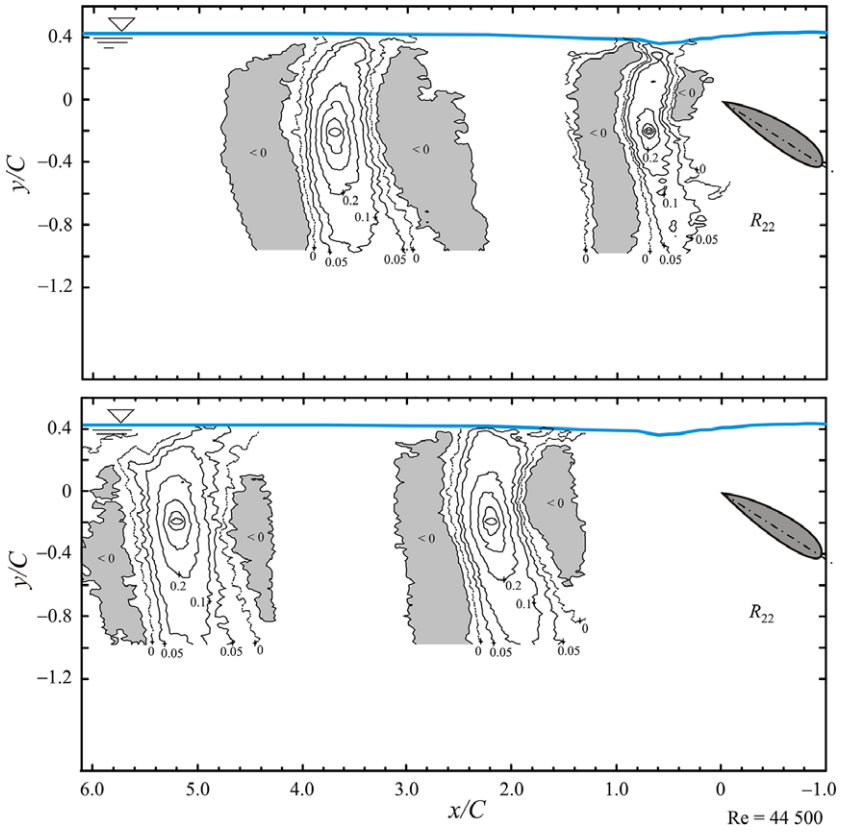

Fig. 13. Correlations for the transverse fluctuating velocity computed at $x/C = 0.7, 2.2, 3.7, 5.2$ for points along the axis of the wake.

and in non-dimensional normalised form becomes

$$R_{ij}(\mathbf{x}, \mathbf{x}+\mathbf{r}) = \frac{\overline{U_i'(\mathbf{x})U_j'(\mathbf{x}+\mathbf{r})}}{\left(\overline{U_i'^2(\mathbf{x})}\,\overline{U_j'^2(\mathbf{x}+\mathbf{r})}\right)^{1/2}}. \tag{13}$$

Having only two-dimensional measurements and neglecting $i \neq j$ implies that only two terms of the correlation tensor can be analysed:

$$R_{11}(x_0, y_0, x_1, y_1) = \overline{U'(x_0, y_0)U'(x_1, y_1)}/\left(\overline{U'^2(x_0, y_0)}\,\overline{U'^2(x_1, y_1)}\right)^{1/2} \quad \text{and}$$

$$R_{22}(x_0, y_0, x_1, y_1) = \overline{V'(x_0, y_0)V'(x_1, y_1)}/\left(\overline{V'^2(x_0, y_0)}\,\overline{V'^2(x_1, y_1)}\right)^{1/2},$$

where (x_0, y_0) is the coordinate of a fixed point and (x_1, y_1) is the coordinate of the variable point. The available data allow the computation of the correlation along the generic directions with fairly good accuracy. In Fig. 12 and in Fig. 13, the contour maps of R_{11} and R_{22} are shown for points along the axis of the wake at four locations downstream: $x/C = 0.7, 2.2, 3.7, 5.2$.

The first attempt to interpret these functions by considering the effects of the eddies described by Townsend [21] was performed by Grant [1], who also measured in the third dimension and found that, in eddies in the wake of a cylinder with circulation and in the x–z plane, counter-rotating couples appear. By limiting the present analysis to two dimensions, a single eddy with velocity components only in the x–y plane results in the following correlation:

$$\chi_{22}(x_0, y_0+\zeta) = \frac{1}{2}A\alpha^2\left(1-\frac{1}{2}\alpha^2\zeta^2\right)\exp\left(-\frac{1}{4}\alpha^2\zeta^2\right), \tag{14}$$

where A specifies the intensity of the eddy and α is a measure of the size of the eddy. For a sequence of eddies located at the same abscissa but at different transverse position, the autocorrelation is:

$$\chi_{22}(x_0, y_0+\zeta) = \sum_i \frac{1}{2}A_i\alpha_i^2\left[1-\frac{1}{2}\alpha_i^2(\zeta-b_i)^2\right] \times \exp\left[-\frac{1}{4}\alpha_i^2(\zeta-b_i)^2\right], \tag{15}$$

where b_i is the shift of the ith eddy. A non-linear least square fitting algorithm for a set of four eddies gives the curve shown in Fig. 14 with a coefficient of determination $R^2 = 0.89$. A similar methodology was also adopted in [19].

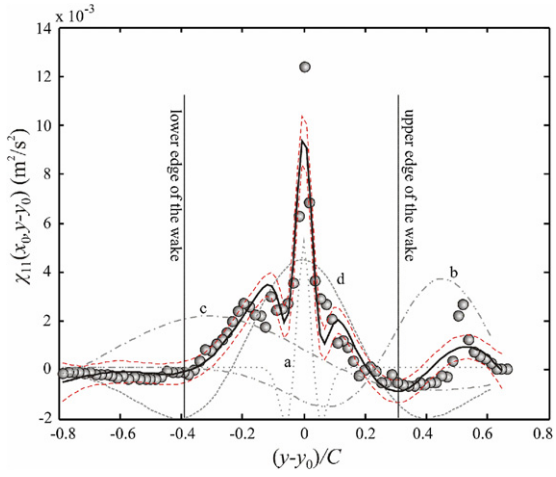

Fig. 14. Correlation $\chi_{11}(x_0, y-y_0) = \overline{U'(x_0, y_0)U'(x_0, y-y_0)}$ at $x_0/C = 0.7$ for a point along the axis of the wake ($y_0/C = -0.32$) fit with 95% prediction bounds. The dotted line, the dash–dot–dot, the dash–dot and the dashed lines are the contributions of the four eddies indicated by the letters **a**, **b**, **c** and **d**.

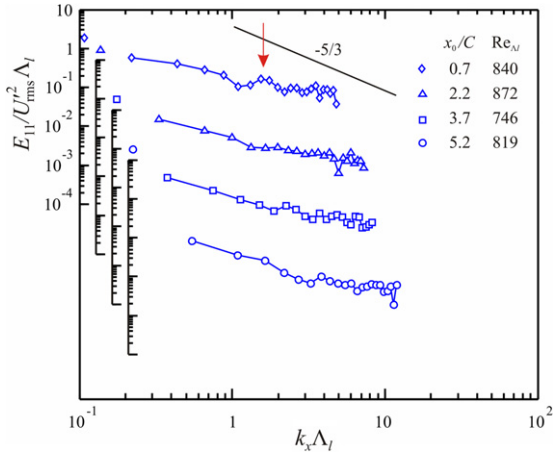

Fig. 15. Longitudinal spectrum at different locations downstream. The arrow indicates the bump of the spectrum due to a family of eddies. For clarity, the curves are translated and refer to different vertical axes.

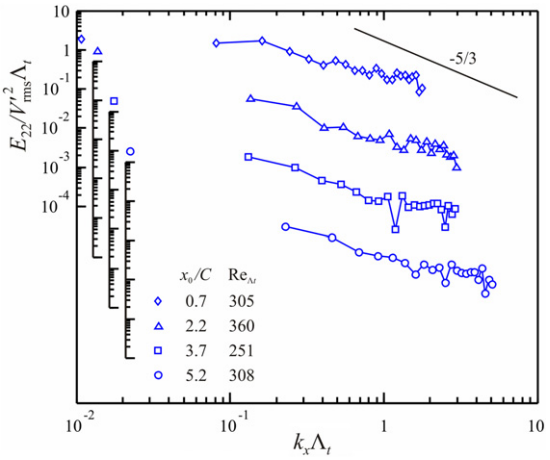

Fig. 16. Transverse spectrum at different locations downstream. For clarity, the curves are translated and refer to different vertical axes.

The four eddies, the separated contributions of which are indicated by the letters **a**, **b**, **c** and **d** in Fig. 14, have centres at $b = 0.1$, 50.2, −29.1, 2.5 mm, size parameters $\alpha = 0.289$, 0.044, 0.023, 0.041 mm^{-1} and non-dimensional coefficients (proportional to the energy per unit volume and the mass density) $(1/2)A_i\alpha_i^2/U_{rms}^{\prime 2} = 0.43, 0.30, 0.18, 0.373$. The eddy indicated with letter **a** is the smallest and is essentially representative of the small-scale turbulence, whereas the other three eddies are large eddies according to the initial characterisation of the flow field. The function is a composite with a large curvature near the origin (eddy **a**), which is typical of large Reynolds number flows, and the smooth portion is due to macro-eddies (the other three eddies). The energy density is comparable for the four eddies. A similar fitting can be obtained for the other components of the correlation function (not shown).

The longitudinal spectrum in the wavenumber domain, defined as

$$E_{11}(k_x) = \frac{1}{\pi}\int_{-\infty}^{\infty} \chi_{11}(x)\exp(-ik_x x)\,dx \tag{16}$$

and the transverse spectrum, defined as

$$E_{22}(k_x) = \frac{1}{\pi}\int_{-\infty}^{\infty} \chi_{22}(x)\exp(-ik_x x)\,dx \tag{17}$$

can be computed by direct integration of the longitudinal and the transverse correlation. The minimum wavenumber is given by the maximum extent of the grid of measurements. Because each FOV is a different realisation of the experiments, the spatial correlations and the spectra are limited to the grid corresponding to a single FOV having approximate size 180 × 150 mm (W, H). Choosing the point (x_0, y_0) along the centreline of the wake in the mid position of the grid results in a spatial extension equal to ≈90 mm in the longitudinal direction and ≈65 mm in the transverse direction. In most cases, the experimental spectra in the wavenumber domain are obtained by pointwise measurements in time and transformed by adopting Taylor's hypothesis for frozen turbulence, but in the present experiments the results are true spectra in the wavenumber domain. The smaller significant wavenumber resolved is equal to $k_{x\min} = 2\pi/0.18 \approx 35$ m^{-1}. The cut-off wavenumber is related to the size of the interrogation window (if a minimum overlap between the interrogation windows is present) and has a value equal to [22]

$$k_{xc} = \frac{2.8}{X_W} \equiv \frac{2.8}{32 \times 0.11 \times 10^{-3}} \approx 795 \text{ m}^{-1}, \tag{18}$$

where X_W is the horizontal size of the interrogation window. The dissipation scale is not achieved. The bandwidth of the computed spectrum is equal to $k_{x\min}$. The spectra at different locations downstream are shown in Fig. 15 and in Fig. 16, are non-dimensional with respect to the integral longitudinal and transverse length scales, which are defined, respectively, as

$$\Lambda_l = \frac{1}{2}\int_{-\infty}^{\infty} R_{11}(x - x_0, y_0)\,dx,$$
$$\Lambda_t = \frac{1}{2}\int_{-\infty}^{\infty} R_{22}(x - x_0, y_0)\,dx. \tag{19}$$

In the longitudinal spectrum immediately downstream from the trailing edge, there is evidence of at least one family of eddies that peak at lengths on the order of the longitudinal integral scale. Similar behaviour can also be detected in the transverse spectra. The Reynolds number is very limited and is more than two orders of magnitude less than the value of 10^5, which is considered as the entry value for the inertial subrange [23]; hence, no inertial subrange behaviour is expected.

4. Conclusion

- Due to the specific geometry of the hydrofoil, the mean flow shows two relevant patterns: the classical wake past the hydrofoil and a breaker at the interface. The breaker also triggers some stationary waves that affect the flow field at several chord lengths downstream. The wake shows a typical defect velocity that is reduced downstream. A vorticity develops at the edges of the hydrofoils as well as at the toe of the breaker, with a persistent pattern downstream. The r.m.s. vorticity is much greater than the average vorticity, especially far downstream where the average vorticity decays.
- The fluctuating longitudinal and transverse velocities have maxima at the wake edges and beneath the breaker. The Reynolds shear stress shows a similar behaviour. The quadrant analysis reveals the dominant contributions of the Q2–Q4 quadrants for the upper lobe and of the Q1–Q3 quadrants for the lower lobe. This behaviour is more evident if a threshold $H = 1$ is imposed to select only events of a fixed intensity.
- The spatial correlation of the fluctuating velocity has been computed for four points on the axis of the wake at locations downstream. The correlation for the longitudinal fluctuating velocity is increasingly isotropic in the far section. The correlation for the transverse fluctuating velocity is clearly anisotropic and decays faster in the longitudinal directions, resulting in negative values as well. The associated integral length scales increase downstream. The longitudinal correlation in the transverse direction can be fitted with a limited number of eddies, with a

clear identification of large eddies and a single main turbulence-associated eddy. Such a pattern requires a very stable and repetitive series of eddies.

- By directly transforming the correlations, the longitudinal and transverse spectra in the wavenumber domain are computed. The longitudinal spectrum in the nearest downstream location shows stronger evidence than the correlation for the existence of large eddies. No inertial subrange is expected because the Reynolds number is quite limited.
- The results of the present tests give a set of data useful for the calibration of numerical models in complex flow-fields, where the presence of an interface makes useless many of the simplifications usually introduced in the model.

Acknowledgements

The experimental activity was carried out at the Laboratory of Hydraulics, Department of Civil Engineering, University of Parma during the brief stay of Francisco Domínguez Luque as a Ph.D. student from the University of Cordoba from the beginning of May to the end of July 2011. The collaboration was arranged through the Cooperation Protocol between the University of Parma and the University of Cordoba. THE PIV was kindly lent by Alessandro Valiani, University of Ferrara. This paper was partially written while Sandro Longo was a visitor at the Cambridge University Engineering Department, Cambridge, UK and was kindly hosted by Dongfang Liang and a by-fellow at Churchill College, Cambridge.

References

[1] H.L. Grant, The large eddies of turbulent motion, J. Fluid Mech. 4 (1958) 149–190.
[2] J.F. Keffer, The uniform distortion of a turbulent wake, J. Fluid Mech. 22 (1965) 135–159.
[3] G.L. Brown, A. Roshko, On density effects and large structure in turbulent mixing layers, J. Fluid Mech. 64 (1974) 775–816.
[4] D.H. Peregrine, Mechanisms of wave breaking, in: M.L. Banner, R.H.J. Grimshaw (Eds.), Proc. IUTAM Symp. on Breaking Wawes, Springer, 1992.
[5] M.L. Banner, D.H. Peregrine, Wave breaking in deep water, Annu. Rev. Fluid Mech. 25 (1993) 373–397.
[6] J.H. Duncan, An experimental investigation of breaking waves produced by a towed hydrofoil, Proc. R. Soc. Lond. Ser. A 377 (1981) 331–348.
[7] J.A. Battjes, T. Sakai, Velocity field in a steady breaker, J. Fluid Mech. 111 (1981) 421–438.
[8] M.L. Banner, The influence of wave breaking on the surface pressure distribution in wind-wave interactions, J. Fluid Mech. 211 (1990) 463–495.
[9] J.C. Lin, D. Rockwell, Evolution of a quasi-steady breaking wave, J. Fluid Mech. 302 (1995) 29–44.
[10] M. Raffel, C.E. Willert, S.T. Wereley, J. Komphenans, Particle Image Velocimetry, Springer, 2007.
[11] D. Liang, C.B. Jiang, Y.L. Li, Cellular neural network to detect spurious vectors in PIV data, Exp. Fluids 34 (2003) 52–62.
[12] C. Shih, C.-M. Ho, Vorticity balance and time scales of a two-dimensional airfoil in an unsteady free stream, Phys. Fluids 6 (2) (1994) 710–723.
[13] W.W. Willmarth, S.S. Lu, Structure of the Reynolds stress near the wall, J. Fluid Mech. 55 (1972) 65–92.
[14] R.J. Alfredsson, A.V. Johansson, On the detection of turbulence-generating events, J. Fluid Mech. 139 (1) (1984) 325–345.
[15] R.S. Brodkey, J.M. Wallace, H. Eckelmann, Some properties of truncated turbulence signals in bounded shear flows, J. Fluid Mech. 63 (1974) 209–224.
[16] R.A. Antonia, L.W.B. Browne, Quadrant analysis in the turbulent far-wake of a cylinder, Fluid Dyn. Res. 2 (1987) 3–14.
[17] K.P. Nolan, E.J. Walsh, D.M. McEligot, Quadrant analysis of a transitional boundary layer subject to free-stream turbulence, J. Fluid Mech. 658 (2010) 310–335.
[18] S. Longo, M.A. Losada, Turbulent structure of air flow over wind-induced gravity waves, Exp. Fluids 53 (2012) 369–390.
[19] S. Longo, L. Chiapponi, M. Clavero, T. Mäkelä, D. Liang, Study of the turbulence in the air-side and water-side boundary layers in experimental laboratory wind induced surface waves, Coast. Eng. 69 (2012) 67–81.
[20] S. Longo, Wind-generated water waves in a wind tunnel: free surface statistics, wind friction and mean air flow properties, Coast. Eng. 61 (1) (2012) 27–41.
[21] A.A. Townsend, The Structure of Turbulent Shear Flow, Cambridge University Press, Cambridge, 1956.
[22] J.M. Foucaut, J. Carlier, M. Stanislas, PIV optimization for the study of turbulent flow using spectral analysis, Meas. Sci. Technol. 15 (2004) 1046–1058.
[23] H. Tennekes, J.L. Lumley, A First Course in Turbulence, MIT Press, 1972.